iScience

Article

Metabolic alterations and immune heterogeneity in gastric cancer metastasis

Graphical abstract

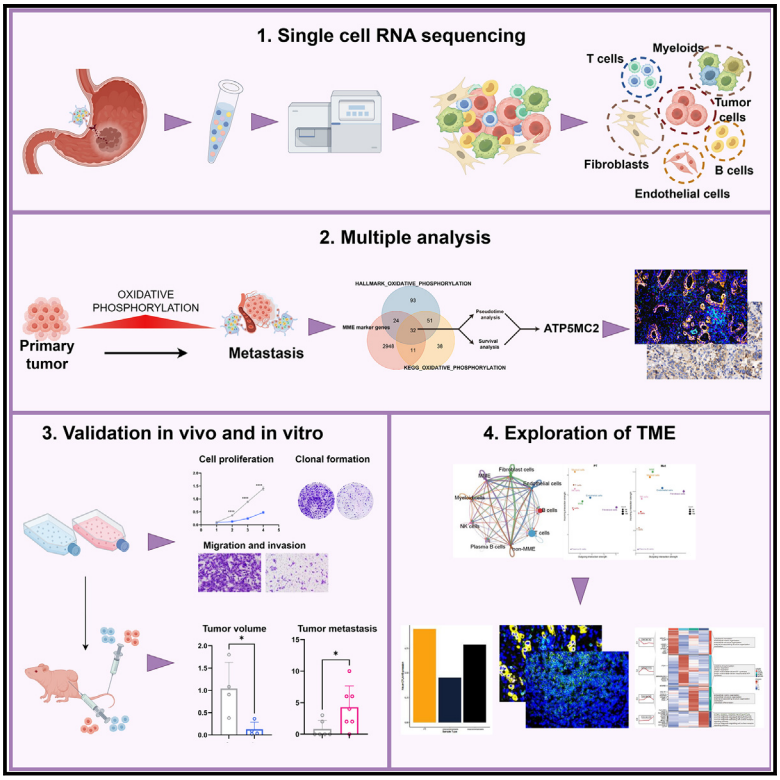

Highlights

- ATP5MC2 uniquely alters during early gastric cancer metastasis
- ATP5MC2 may drives metastasis via oxphos reprogramming in gastric cancer
- Single-cell atlas reveals immune heterogeneity linked to gastric cancer metastasis

Authors

Rui Zeng, Zhihao Lin, Feiyan Feng, ..., Yan Mei, Hongmei Wu, Qingling Zhang

Correspondence

meiyan@gdph.org.cn (Y.M.), wuhongmei@gdph.org.cn (H.W.), zhangqingling@gdph.org.cn (Q.Z.)

In brief

Microenvironment; Immunology; Cell biology; Cancer

Zeng et al., 2025, iScience *28*, 112296
May 16, 2025
https://doi.org/10.1016/j.isci.2025.112296

CellPress

iScience

CellPress
OPEN ACCESS

Article

Metabolic alterations and immune heterogeneity in gastric cancer metastasis

Rui Zeng,[1,2,3,5] Zhihao Lin,[1,2,3,5] Feiyan Feng,[2,3,5] Yanyan Li,[1,2,3] Weiwei Liu,[2,3] Wenting He,[2,3] Yongjun Huang,[2,3] Xingtao Lin,[2,3] Yan Mei,[2,3,*] Hongmei Wu,[2,3,*] and Qingling Zhang[4,*]

[1]School of Medicine, South China University of Technology, Guangzhou 510006, China

[2]Department of Pathology, Guangdong Provincial People's Hospital (Guangdong Academy of Medical Sciences), Guangzhou 510080, China

[3]Guangdong Provincial Key Laboratory of Artificial Intelligence in Medical Image Analysis and Application, Guangdong Provincial People's Hospital, Guangdong Academy of Medical Sciences, Guangzhou 510080, China

[4]Department of Pathology, Guangdong Provincial People's Hospital (Guangdong Academy of Medical Sciences), Guangzhou, 510080, China; Guangdong Provincial Key Laboratory of Artificial Intelligence in Medical Image Analysis and Application, Guangdong Provincial People's Hospital (Guangdong Academy of Medical Sciences), Guangzhou, 510080, China; School of Medicine, South China University of Technology, Guangzhou 510006, China

[5]These authors contributed equally

*Correspondence: meiyan@gdph.org.cn (Y.M.), wuhongmei@gdph.org.cn (H.W.), zhangqingling@gdph.org.cn (Q.Z.)

https://doi.org/10.1016/j.isci.2025.112296

SUMMARY

Cellular metabolic reprogramming supports tumor proliferation, invasion, and metastasis by enhancing resistance to stress and immune clearance. Understanding these metabolic changes within the tumor microenvironment is vital to developing effective therapies. We conducted single-cell RNA sequencing on 11 gastric cancer (GC) samples and eight metastatic lesions, analyzing 92,842 cells across eight cell types, including cancer cells, stromal cells, and immune cells. Our findings highlight that the mitochondrial ATP synthase subunit ATP5MC2 uniquely alters during early GC metastasis. Experiments and clinical data confirmed that ATP5MC2 upregulation facilitates cancer cell proliferation, invasion, and metastasis. Constructing a single-cell atlas revealed significant immune cell heterogeneity associated with GC metastasis and its molecular subtypes. This study underscores the role of ATP5MC2-driven metabolic changes and diverse immune landscapes in promoting GC metastasis, offering new avenues for anti-metastatic treatment development.

INTRODUCTION

Gastric cancer (GC) has the highest incidence among malignant tumors of the digestive tract. It is the fifth most common malignancy and the fourth leading cause of cancer-related deaths worldwide[1] due to the lack of specific clinical symptoms in the early stages of GC and the absence of susceptible diagnostic methods. Cancer cells with metastatic potential and micro-metastatic lesions often go undetected, leading to the majority of patients being diagnosed at an advanced stage.[2] Metastasis is a major cause of treatment failure in GC. Advanced GC is often accompanied by lymph node or surrounding organ metastasis, and some patients may even develop distant metastases.[3] Therefore, exploring the mechanisms of GC metastasis is crucial for developing new therapeutic strategies.

GC cells, originating from gastric epithelium, exhibit metabolic characteristics similar to other types of tumors, preferring glycolysis over the tricarboxylic acid cycle to obtain energy, a phenomenon known as the Warburg effect.[4] Recent studies suggest that metabolic alteration in metastatic cancer cells serves purposes beyond meeting the escalating energy demands through the Warburg effect, it also contributes to immune evasion and the formation of pre-metastatic niches. Li et al. reported that the metastatic process in lymph nodes involves enhanced oxidative phosphorylation and increased ATP consumption, indicating that metabolic alteration is crucial in preparing metastatic cells for pre-metastatic niche formation.[5] Other studies have shown that when glycolytic energy supply is insufficient, the decrease in fructose-1,6-bisphosphate (FBP) indirectly activates the Adenosine 5 '-monophosphate-activated protein kinase (AMPK) pathway, which in turn downregulates mTORC1 and HIF-1α expression, suppressing the differentiation of dendritic cells (DCs) and effector T cells (Teff) and thereby promoting immune escape in tumor cells.[6] However, the specific metabolic adaptations during GC metastasis remain largely unknown. Given the high heterogeneity of GC, the metabolic patterns involved in metastasis are also highly variable, and current evidence is insufficient to support the development of targeted therapies to block lymph node metastasis in GC. Single-cell RNA sequencing (scRNA-seq) technology allows for the specific analysis of cell populations within the highly complex tumor microenvironment (TME) at the single-cell level. This technology not only reveals previously uncharacterized molecular complexities within tumor cells but also explores the roles of major cell types in the tumor immune microenvironment, such as T cells, B cells, macrophages, endothelial cells, and fibroblasts, in the development and metastasis of GC.[7]

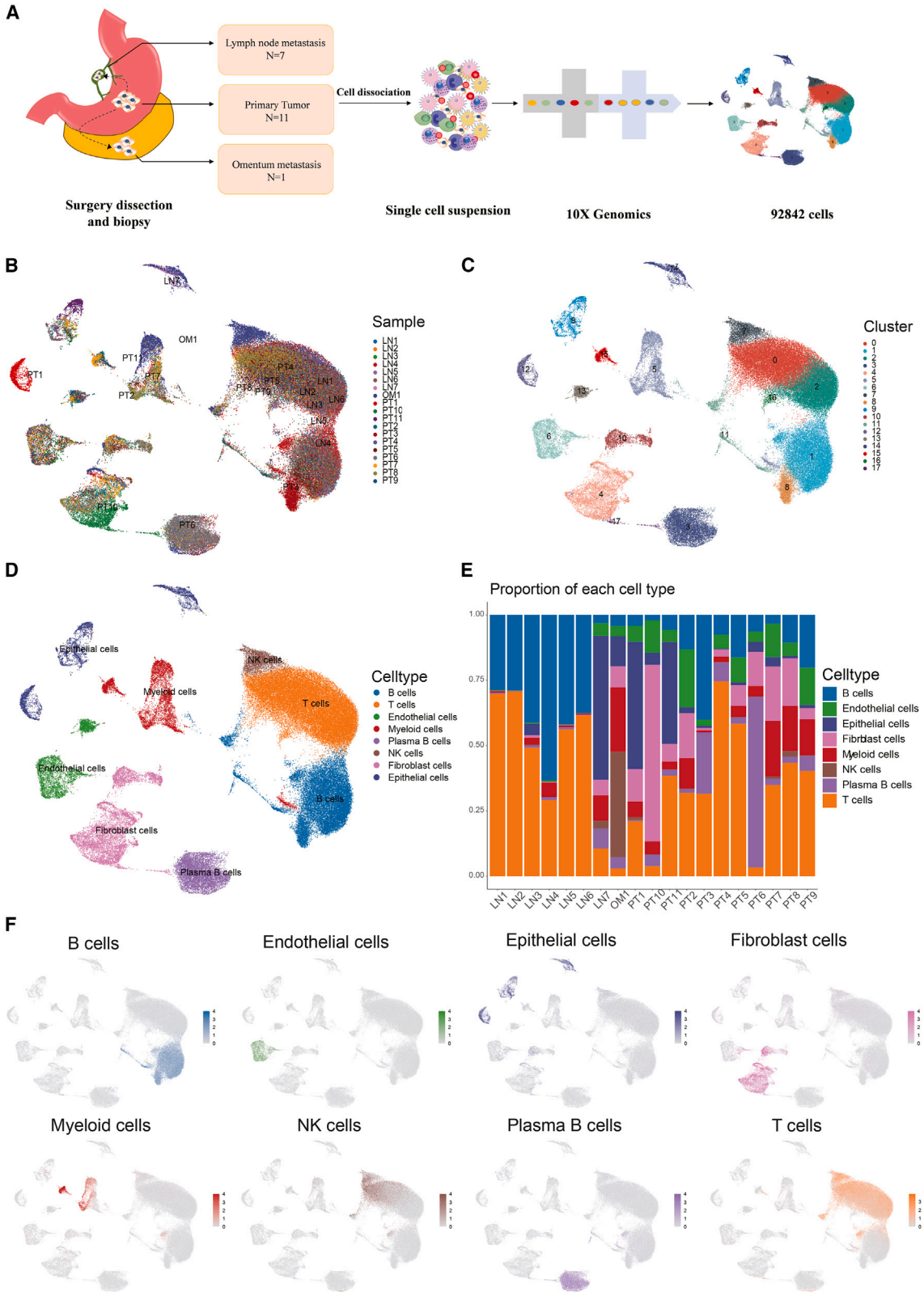

(legend on next page)

This study leveraged scRNA-seq to provide a detailed characterization of the heterogeneity and metabolic adaptations occurring from primary to metastatic GC. One of the central innovations of our research is the identification of ATP5MC2 as a driver of metastasis in GC, enhancing malignant properties such as cancer cell proliferation, migration, and invasiveness. Unlike previous studies that primarily focused on metabolic alterations in primary GC cells, our work reveals the dynamic changes in tumor cells and the TME throughout the metastatic process, illustrating how internal drivers and interactions among diverse microenvironmental components support tumor progression and metastasis. These findings not only position ATP5MC2 as a potential target for inhibiting GC metastasis but also provide a valuable reference for understanding the complex intercellular dynamics during metastasis, addressing gaps in our current understanding of GC metastasis.

RESULTS

The scRNA-seq atlas of GC primary tissues and lymph nodes

In this study, we conducted single-cell RNA-seq analysis on 19 fresh samples from 12 GC patients, including 11 primary tumors (PTs), 7 paired lymph nodes (LNs) (4 of which exhibited metastasis upon histological evaluation), and 1 omental metastasis (OM) (Table S1). After rigorous quality control, we profiled the transcriptomes of 92,842 cells across these samples (Figures 1A and 1B). Following the removal of batch effects, dimensionality reduction, and unsupervised clustering, we identified 18 distinct subpopulations (Figure 1C). Using cell-specific marker genes (Figure S1A) and the PanglaoDB database,[8] these cells were classified into eight cell types: epithelial cells, lymphocytes (T, B, and natural killer [NK] cells), plasma cells, stromal cells (fibroblasts and endothelial cells), and myeloid cells (Figures 1D and 1F). The analysis revealed significant heterogeneity among these cells, underscoring their complex functional roles within the TME (Figure 1E).

Comparative analysis of cellular composition between PT and LN samples showed a significant enrichment of T cells, fibroblasts, and myeloid cells in PT samples, while B cells were more enriched in LN samples (Figures 1E and S1B). The higher heterogeneity observed in PT samples compared to LN samples suggests substantial modulation of the TME by tumor subtypes (Figure 1E).

Elevated CNV levels and enhanced intercellular interactions in MME cells

Given that GC originates from epithelial cells, we focused on epithelial cells for re-dimensionality reduction and clustering, which resulted in the identification of 15 subgroups (Figure 2A). We then analyzed the composition of epithelial cells in each sample (Figure 2B). Malignant epithelial cells exhibited higher copy number variation (CNV) levels compared to non-malignant epithelial cells. To differentiate between malignant and non-malignant clusters, we evaluated the CNV levels across all epithelial cell clusters, revealing varying CNV levels among the clusters (Figures 2C and S2A).

To further distinguish malignant from non-malignant cells, we conducted pseudotime analysis on the epithelial cells. The results indicated two distinct cell fates: cell fate 1, primarily composed of cells from clusters 1 and 3, and cell fate 2, primarily composed of cells from clusters 2 and 4 (Figure 2D). Based on the results of CNV analysis and pseudotime analysis, cluster 0 was identified as representing normal gastric epithelial cells, as it was located at the starting point of the pseudotime trajectory and exhibited significantly lower CNV levels. In contrast, clusters 1, 2, 3, and 4, which displayed higher CNV levels, were classified as tumor cells. This suggests that tumor cells within the GC microenvironment follow two distinct evolutionary trajectories.

Since clusters 1 and 3 were primarily located in lymph nodes and clusters 2 and 4 were mainly found at the PT site, we designated cell fate 1 as the metastatic pathway and cell fate 2 as the primary site evolution trajectory. Accordingly, we defined clusters 1, 3, and 12, located at the end of the cell fate 1, as metastatic malignant epithelial (MME) cells. The UMAP plot illustrates the distribution of MME cells among the epithelial cells (Figure 2E). Additionally, we compared the CNV levels between non-MME and MME cells, finding that MME cells had significantly higher CNV levels, indicating a higher degree of malignancy (Figure 2F).

To investigate how the interactions between MME and immune or stromal cells in the microenvironment differ between primary and metastatic sites, we performed CellChat analysis to predict intercellular communication. Active signaling was observed among various cell types associated with MME, including T cells, B cells, myeloid cells, NK cells, endothelial cells, and fibroblasts, with the number and intensity of interactions summarized in Figure 2G. When comparing primary and metastatic sites, we observed a significant increase in both the number and intensity of cell-cell interactions in metastatic sites, particularly the interaction intensity (Figures 2H and S2F). Notably, MME-derived signaling to stromal cells (endothelial cells and fibroblasts) was markedly enhanced in metastatic sites, while signaling to T cells was significantly reduced, indicating stronger metastatic and immunosuppressive properties of MME in these sites (Figure 2I). Additionally, the input and output signaling activity of various cell types in metastatic lesions was more pronounced compared to primary lesions, suggesting that MME, as an "outsider," exerts a potent remodeling effect on the lymph node microenvironment (Figures 2J and S2G).

Figure 1. Cellular overview of the gastric primary tumor (PT), lymph node (LN), and omentum metastasis (OM)

(A) Study overview.

(B) A total of 19 samples from PT (n = 11), LN (n = 7), and OM (n = 1) yielded 92,842 cells through 10× Genomic sequencing.

(C) UMAP plot displaying the distribution of 92,842 cells, colored by clusters.

(D) UMAP plot displaying 92,842 cells, colored by their eight major cell types.

(E) The stack diagram shows the cell type composition of each sample.

(F) UMAP visualization of all cell types.

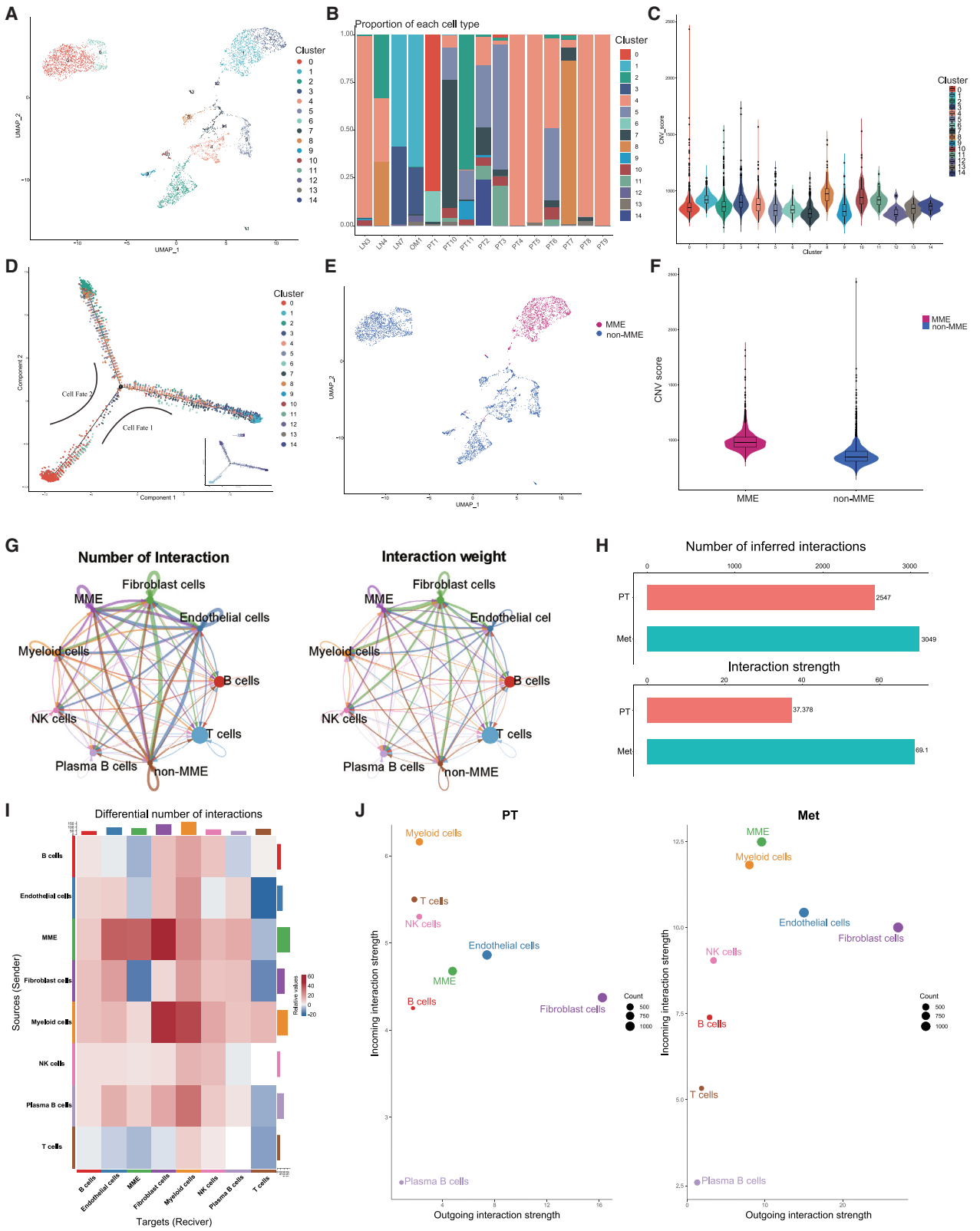

(legend on next page)

Abnormal metabolic shifts in malignant epithelial cells during tumor metastasis

To explore the driving forces that lead GC away from the primary site and into the metastasis pathway, we used Hallmark gene sets of the Molecular Signatures Database (MsigDB) to explore the pathway that presents significant differences between cell fate1 and cell fate 2.

Most of the gene sets in the Hallmark collection exhibited similar pseudotime sequence changes in both cell fates. However, oxidative phosphorylation followed distinct pseudotime trajectories in the two cell fates. Specifically, in cell fate 1, which represents tumor metastasis, oxidative phosphorylation initially increased and then decreased, drawing our attention (Figure 3A). To explore this further, we divided the TCGA-STAD (TCGA: The Cancer Genome Atlas) cohort with metastasis into four grades (N1–N4) and calculated the oxidative phosphorylation score. The results, derived from two different gene sets, consistently demonstrated that oxidative phosphorylation initially increased and then decreased during the metastatic process (Figure 3B). Additionally, UMAP revealed that MME cells have higher oxidative phosphorylation scores (Figure S2B). Correspondingly, pseudotime analysis showed that cell fate 1 also exhibited higher oxidative phosphorylation scores (Figure S2C). Gene set variation analysis (GSVA) analysis further confirmed MME cells (clusters 1, 3, and 12) had elevated oxidative phosphorylation scores, with cluster 1 showing lower glycolysis scores (Figure S2E). Then, we intersected the gene concentrated in HALLMARK_ OXIDATIVE_PHOSPHORYLATION and KEGG_ OXIDATIVE_ PHOSPHORYLATION with the marker gene of MME (KEGG: Kyoto Encyclopedia of Genes and Genomes) (Figure 3C). To further clarify the research significance of the 32 intersecting genes, we performed pseudotime trajectory and survival analyses, identifying ATP5MC2 as the only gene with a pseudotime trajectory highly consistent with the oxidative phosphorylation pathway across both cell fate trajectories and a significant correlation with survival (Figure 3C). Specifically, to assess ATP5MC2's prognostic value, we analyzed data from the TCGA-STAD cohort, which includes 293 samples with survival information. We not only found that ATP5MC2 was significantly overexpressed in tumor samples (Figure S2D), but also found that the overall survival was significantly worse in the group with high expression of ATP5MC2 (Figure 3E). We further evaluated the ATP5MC2 expression in TME via multiplex immunofluorescence of PanCK, CD3, CD20, and SMA. Our findings revealed that ATP5MC2 was co-expressed with PanCK in tumor samples (Figure 3F), indicating that a subset of tumor cells was positive for ATP5MC2.

Clinical samples confirmed the relationship between ATP5MC2 and GC metastasis

Immunohistochemical (IHC) staining was performed on adjacent normal tissue, as well as tumor tissue with and without lymph node metastasis. The results indicated that tumor samples with lymph node metastasis (LN+) exhibited a higher positive rate and immunoreactive score compared to adjacent normal tissue and tumor samples without lymph node metastasis (LN−) (Figures 4A and 4B). Subsequently, we divided the TCGA-STAD cohort into ATP5MC2_Low and ATP5MC2_High groups based on ATP5MC2 expression levels. Gene set enrichment analysis (GSEA) analysis demonstrated a positive correlation between the ATP5MC2_High group and tumor metastasis, while the ATP5MC2_Low group showed the opposite trend (Figure 4C). Additional IHC staining of lymph node samples confirmed that ATP5MC2 expression was positive in samples with lymph node metastasis, with these metastatic lymph nodes showing significantly higher immunoreactive scores Figures 4D and 4E.

ATP5MC2 promotes GC growth and metastasis

We first measured the expression of ATP5MC2 in four different GC cell lines (AGS, N87, MKN45, and HGC27) (Figure 4F) and subsequently generated knockdown and overexpression cell lines using lentiviral transfection (Figures 4G and 4H). We then validated the cellular ATP levels following ATP5MC2 knockdown and overexpression. The results showed that ATP levels significantly decreased after ATP5MC2 knockdown, while overexpression led to a significant increase (Figure 4I). To evaluate the effects of ATP5MC2 knockdown and overexpression on cell viability and proliferation, we conducted CCK-8 and colony formation assays. The results indicated that, compared to the NC group, knockdown of ATP5MC2 significantly inhibited GC cell proliferation (Figure 5A) and colony formation ability (Figure 5B), while overexpression markedly promoted both proliferation and colony formation in GC cells. Additionally, transwell assays demonstrated that ATP5MC2 knockdown effectively inhibited the migration and invasion of AGS (Figure 5C) and HGC27 (Figure 5D) cell lines, while ATP5MC2 overexpression significantly promoted the migration and invasion of the MKN45 cell line (Figure 5E). Consistently, *in vivo* experiments using a mouse subcutaneous xenograft model revealed that ATP5MC2 knockdown effectively inhibited tumor growth (Figure 5F), whereas ATP5MC2 overexpression significantly promoted the growth of subcutaneous xenografts (Figure 5G). Furthermore, compared to the vector group, MKN45 cells with ATP5MC2 overexpression exhibited increased lung metastasis in nude mice (Figures 6A–6E).

Figure 2. Identification of metastatic malignant epithelial (MME) cells

(A) Sub-clustering of epithelial cells, colored and labeled by clusters.
(B) The stack diagram shows the proportion of epithelial cell clusters in each sample.
(C) The violin plot shows the CNV levels in each epithelial cell cluster.
(D) Pseudotime trajectory shows two distinct cell fates of epithelial cells.
(E) UMAP plot displaying epithelial cells colored by non-MME and MME.
(F) The violin plot shows the CNV levels between non-MME and MME epithelial cells.
(G) The circle plot shows the number and weight of cell-cell communications among different cell subpopulations.
(H) Bar plots provide aggregated statistics on the number and intensity of cell-cell interactions between primary (PT) and metastatic (Met) samples.
(I) The heatmap shows changes in intercellular source-target interactions in metastatic (Met) samples compared to primary (PT) samples, with red indicating upregulation and blue indicating downregulation.
(J) Detailed changes in cell-cell signaling between primary (PT) and metastatic (Met) samples.

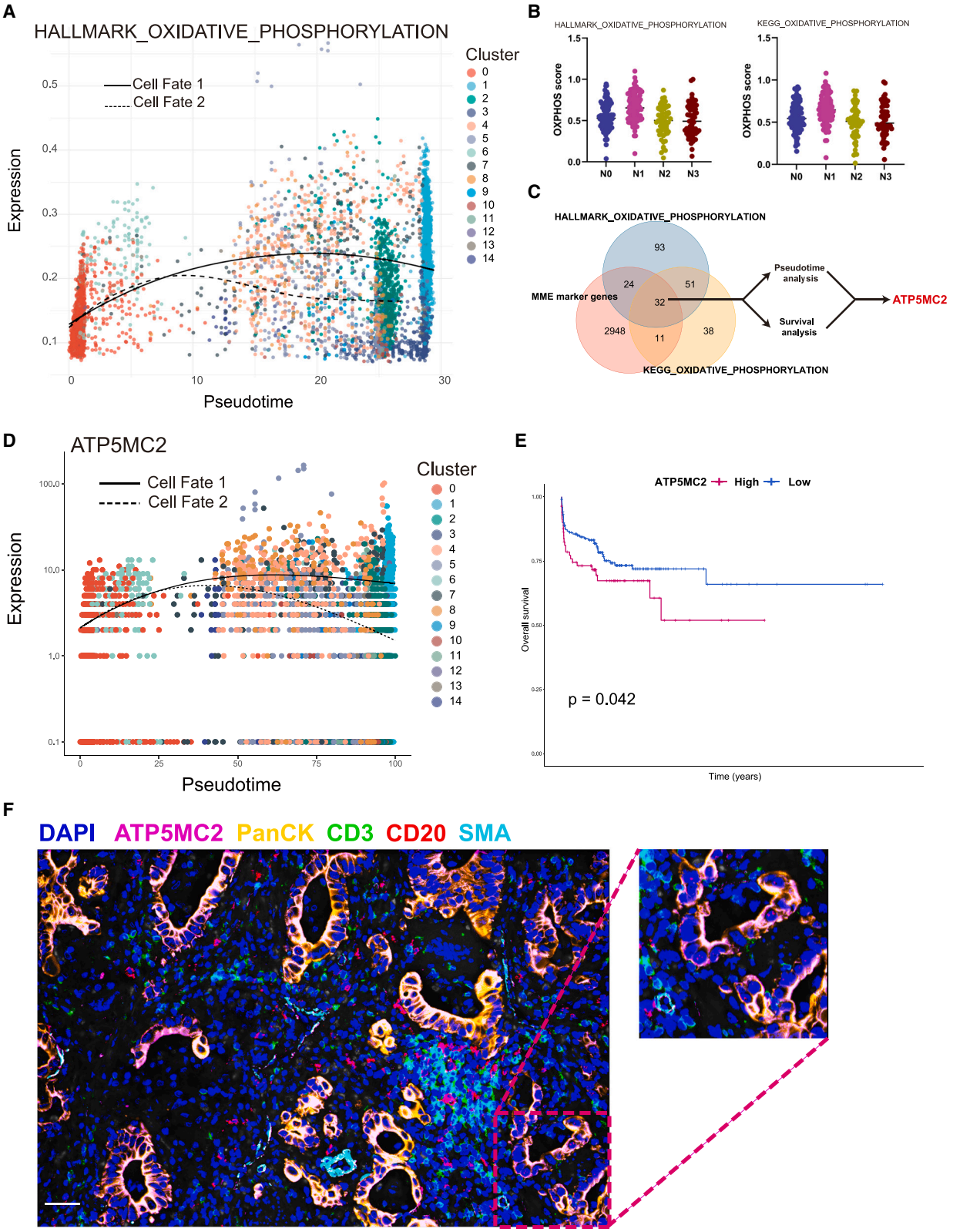

(legend on next page)

Dynamic changes of T cells in the process of tumor metastasis

Some lymph node samples appeared negative for metastasis upon histological examination but still exhibited trace amounts of cancer cells when analyzed by single-cell sequencing. These samples were thus classified as micro-metastasis (Table S1). To investigate whether T cells undergo subtle changes before metastasis occurs, we extracted T cells from all samples for dimensionality reduction and annotation (Figures 7A, 7B, and S3A–S3D). We found a gradual depletion of cytotoxic T lymphocytes (CD8_CTL) and effector memory T cells (CD8_Tem) during the progression from PT to micrometastases and subsequently to large metastases. In contrast, exhausted $CD8^+$ T cells (CD8_Tex) accumulated throughout this metastatic progression. (Figure 7C). Further pseudotime analysis demonstrated that CD8 T cells evolved from naive T cells (CD8_Tn) at the start to exhausted T cells (CD8_Tex) at the end (Figures S3F and S3G). GSEA (Figure 7D) and gene ontology (GO) enrichment analysis (Figures S3H–S3I) of T cells in micro-metastatic and macro-metastatic samples indicated that T cells in micro-metastatic samples were mainly involved in pathways related to T cell activation and immune response, whereas T cells in macro-metastatic samples were primarily associated with cell adhesion regulation, suggesting that T cells may have been reprogrammed by the tumor to promote metastasis.

Additionally, we analyzed the expression of immune checkpoint molecules on T cells at different stages of metastasis. Interestingly, complementing the trend of oxidative phosphorylation in tumor cells, the expression levels of these immune checkpoint molecules on T cells decreased and then increased during metastasis (Figure 7E). A similar trend of exhausted T cells infiltration was observed in the GC and lymph node samples involved in this study using multiplex immunofluorescence (Figure S3J). This led us to hypothesize that, in the early stages of metastasis, tumor cells may undergo reprogramming into "pre-metastatic precursor cells" that resemble normal cells, allowing them to evade immune surveillance and clearance, thereby facilitating successful metastasis. Consequently, T cells in the pre-metastatic microenvironment may also undergo changes, adapting to a microenvironment resembling that of normal tissue. Once metastasis is established, tumor cells revert to their original characteristics, and T cells return to an immunosuppressive state within the TME.

Potential role of lymphatic endothelial cells in promoting metastasis

We next investigated whether the unique characteristics of endothelial cells, as pathways of metastasis, play a critical role in lymphatic metastasis of tumors. To this end, we selected endothelial cells and annotated them as vascular endothelial cells and lymphatic endothelial cells (Figures 7F and 7G). Pseudotime analysis revealed that, although vascular and lymphatic endothelial cells share a common evolutionary origin, lymphatic endothelial cells later formed a distinct branch, indicating differences in their characteristics (Figure 7H). GO enrichment analysis showed that lymphatic endothelial cells are primarily enriched in pathways associated with cell adhesion and the extracellular matrix, suggesting their potential role in promoting metastasis. In contrast, vascular endothelial cells were enriched in pathways associated with leukocyte migration and blood vessel development (Figure 7I).

Microenvironmental heterogeneity across different GC molecular subtypes

Given that our collected samples encompass various molecular subtypes, including microsatellite instability (MSI), chromosomal instability (CIN), Epstein-Barr virus-associated (EBV), and genomically stable (GS) subtypes, we conducted a single-cell analysis of the immune microenvironment in each subtype. Research has shown that EBV-infected B cells can alter germinal center reactions,[9] and the microenvironment of EBV-positive GC exhibits an inflammatory immune phenotype, with increased infiltration of T cells and B cells.[10] Consequently, we performed dimensionality reduction and annotation of B cells (Figures S4A, S4B, and S4D), the heatmap shows the DEGs of each subtype of B cell compared to other subtypes (Figure S4C). UMAP revealed the significant heterogeneity in B cells between EBV− and EBV+ patients (Figure S4E). Further statistical analysis showed that, compared to EBV− patients, EBV+ patients had a higher proportion of germinal center B cells, naive B cells, and plasma cells, along with a corresponding decrease in memory B cells and precursor B cells (Figure S4F). We also calculated germinal center scores for both groups, finding that EBV+ patients exhibited greater germinal center infiltration, which may be associated with better prognostic outcomes[11] (Figure S4G).

Next, we identified tumor-associated macrophages (TAMs) of myeloid origin (Figures S5A–S5C) and classified them into five distinct subpopulations. These included FOLR2+ TAMs, which are associated with pro-inflammatory, anti-tumor responses, and SPP1+ TAMs, which are linked to immunosuppressive functions. A heatmap highlights the DEGs specific to each myeloid cell subtype compared to the others (Figure S5D). SPP1+ TAMs displayed a greater capacity for promoting angiogenesis (Figure S5E), while FOLR2+ TAMs showed higher levels of inflammatory response and inhibition of angiogenesis (Figures S5F and S5G). Additionally, we explored TAM heterogeneity across different molecular subtypes (Figure S5H). The antigen-presenting molecule HLA-DPB1 was more highly expressed in CIN and

Figure 3. The unique expression trend of ATP5MC2 in gastric cancer metastasis

(A) The cells of the two fates have different trajectories of oxidative phosphorylation pathways.

(B) Oxidative phosphorylation scores at different stages (N1–N4) of metastasis in TCGA-STAD cohort.

(C) Venn diagram shows the intersection gene of MME marker genes, HALLMARK_OXIDATIVE_PHOSPHORYLATION and KEGG_OXIDATIVE_PHOSPHORYLATION.

(D) The pseudotime trajectory of ATP5MC2 between two different fate cells.

(E) The Kaplan-Meier curve illustrates that higher ATP5MC2 is associated with poorer survival in gastric cancer.

(F) Multiplex immunofluorescence was utilized to detect ATP5MC2 expression within the microenvironment. Scale bars: 35 μm.

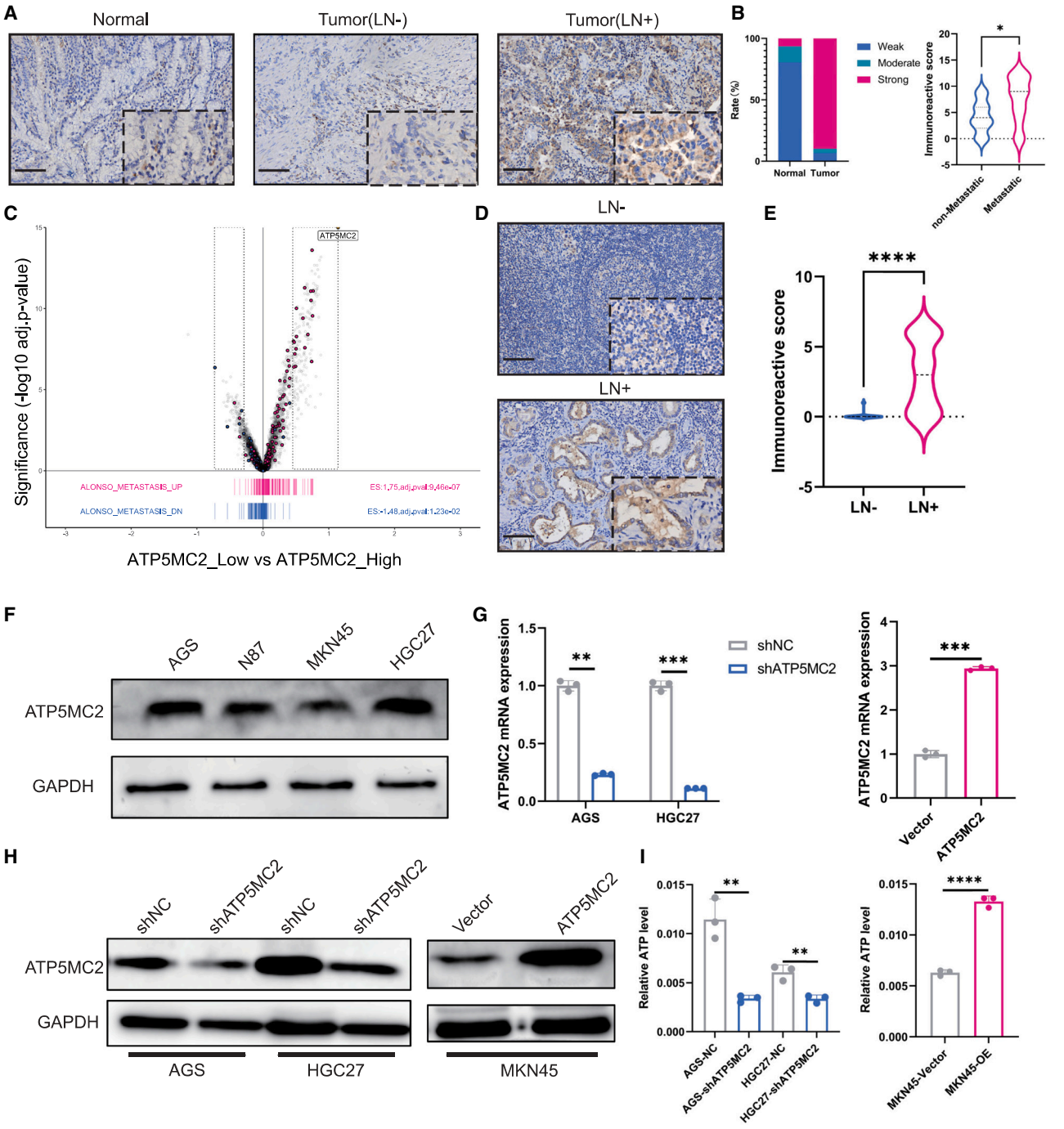

Figure 4. ATP5MC2 upregulation in primary gastric tumors and lymph nodes of patients with metastasis

(A and B) ATP5MC2 expression and statistical analysis in normal, metastatic, and non-metastatic gastric cancer tissues. Scale bars: 100 μm

(C) The high expression of ATP5MC2 in gastric cancer is associated with metastasis.

(D and E) ATP5MC2 expression and statistical analysis in metastatic and non-metastatic lymph nodes. Scale bars: 100 μm

(F) Western blot analyzes ATP5MC2 expression in gastric cancer cell lines.

(G and H) RT-qPCR and western blot verify the knockdown and overexpression effects of ATP5MC2 in gastric cancer cell lines AGS, HGC27, and MKN45.

(I) Intracellular ATP content changes after ATP5MC2 knock down and overexpression. Statistical comparisons between two groups were performed using a t test. Data are represented as mean ± SD.

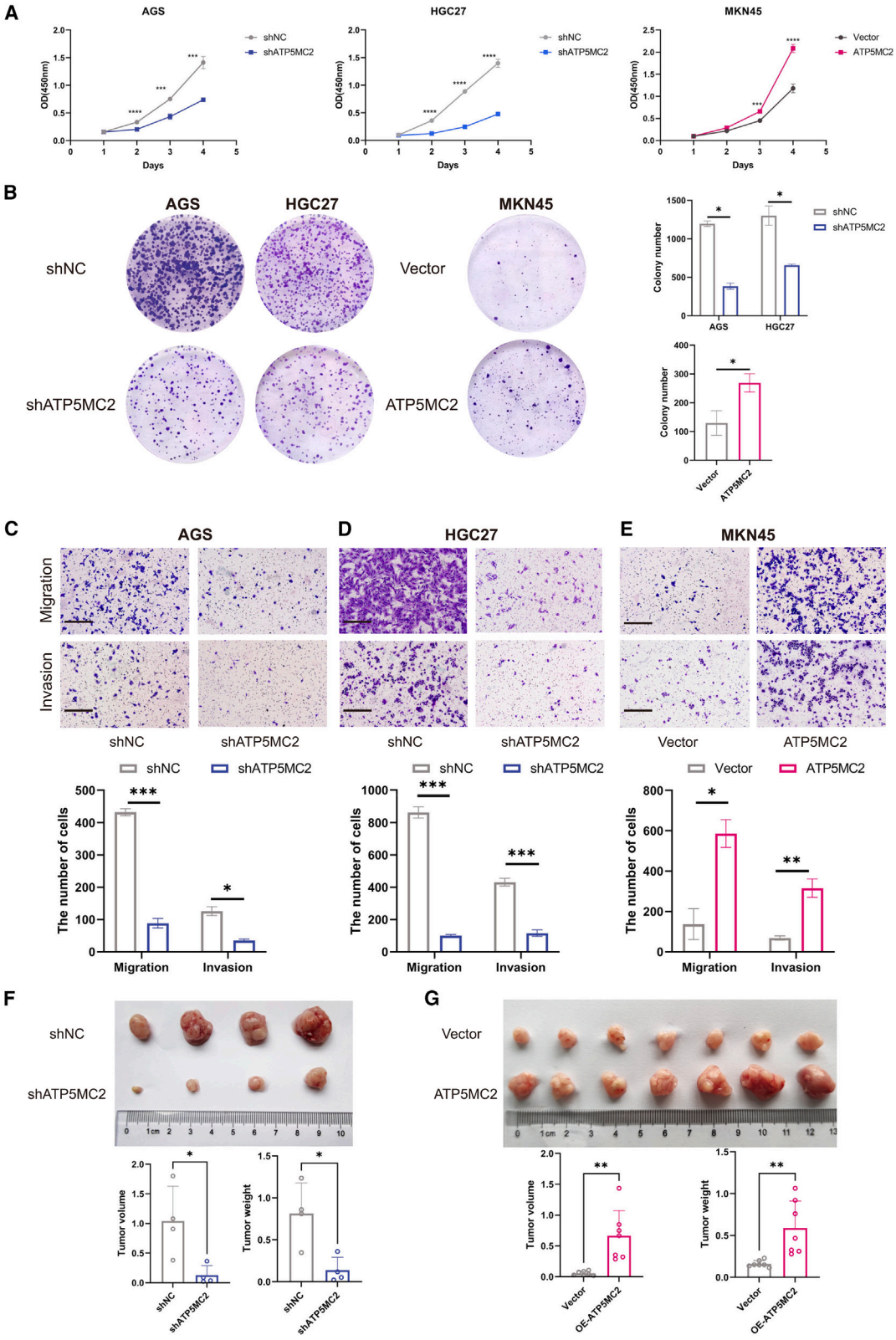

(legend on next page)

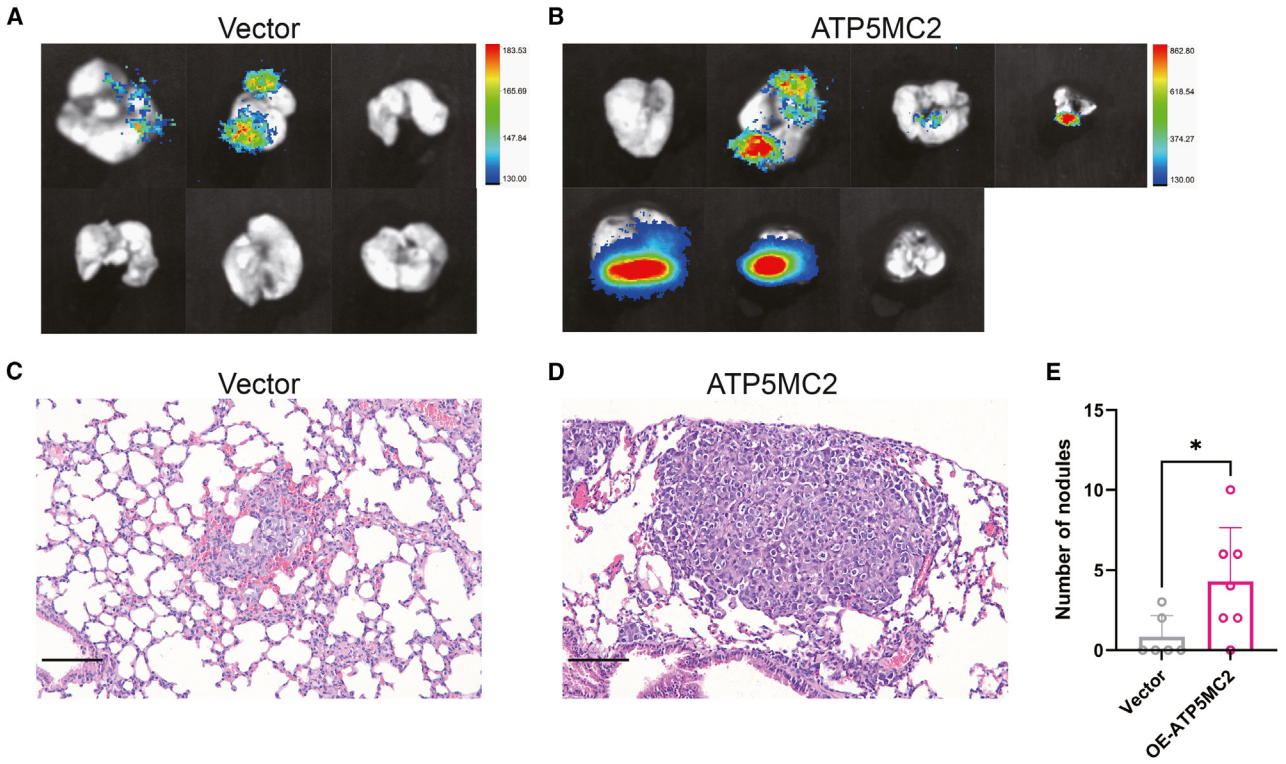

Figure 6. ATP5MC2 overexpression promotes gastric cancer metastasis

(A and B) Lung tumor metastasis in mice injected with ATP5MC2-vector and ATP5MC2-OE MKN45 cells assessed by *ex vivo* bioluminescent assay.

(C and D) Representative images of lung metastases in mice injected with ATP5MC2-vector and ATP5MC2-OE MKN45 cells with H&E staining. Scale bars: 50 μm

(E) Statistical analysis of lung metastases in mice. Statistical comparisons between two groups were performed using a t test. Data are represented as mean ± SD.

GS subtypes (Figure S5I), and the pro-inflammatory cytokine IL-1B, which activates anti-tumor responses, was more highly expressed in EBV and GS subtypes (Figure S5J). In contrast, VEGFA, which promotes angiogenesis, showed no significant differences in expression across the four subtypes (Figure S5K).

Finally, we identified key components of the stromal cells, specifically tumor-associated fibroblasts (CAFs), classifying them into four subpopulations: apCAFs, eCAFs, iCAFs, and mCAFs (Figures S6A–S6C). mCAFs were primarily involved in energy metabolism within muscle cells, while apCAFs were mainly associated with antigen presentation and immune responses. iCAFs and eCAFs were primarily involved in extracellular matrix construction, with their infiltration increasing in the later stages of tumor evolution, potentially related to the processes of tumor metastasis and colonization (Figure S6D).

DISCUSSION

Due to the high heterogeneity of tumors and our limited understanding of the underlying molecular and genetic mechanisms driving disease progression, cancer metastasis remains a significant clinical barrier that severely reduces patient prognosis.[12] Compared to normal cells, the metabolism of cancer cells is more vigorous, with increased glucose consumption promoting aerobic glycolysis, also known as the "Warburg effect."[13–16] Our study found a unique trend in oxidative phosphorylation during GC metastasis: in MME cells, oxidative phosphorylation first increased and then decreased, while in PT cells, the opposite metabolic pattern was observed. This observation aligns closely with recent findings, which suggest that circulating tumor cells (CTCs) may undergo an "anti-Warburg effect," where oxidative phosphorylation replaces glycolysis as the primary metabolic

Figure 5. Deciphering the function of ATP5MC2 in tumor cells

(A) Cell proliferation analyses of AGS, HGC27, and MKN45.

(B) Representative images from colony formation assays for AGS, HGC27, and MKN45 (left) and quantification of colony formation for AGS, HGC27, and MKN45 (right).

(C–E) Transwell analyzes the migration and invasion of AGS (C), HGC27 (D), and MKN45 (E) (up), respectively. Quantifying migration and invasion for AGS, HGC27, and MKN45 (down). Scale bars: 100 μm

(F) Images of gross GC subcutaneous tumors formed by HGC27 (up) and the analyses of volume and weight of GC subcutaneous tumors (down).

(G) Images of gross GC subcutaneous tumors formed by MKN45 (up) and the analyses of volume and weight of GC subcutaneous tumors (down).

Statistical significance for CCK-8 results was determined using two-way ANOVA, while all other results were analyzed using a t test. Data are represented as mean ± SD.

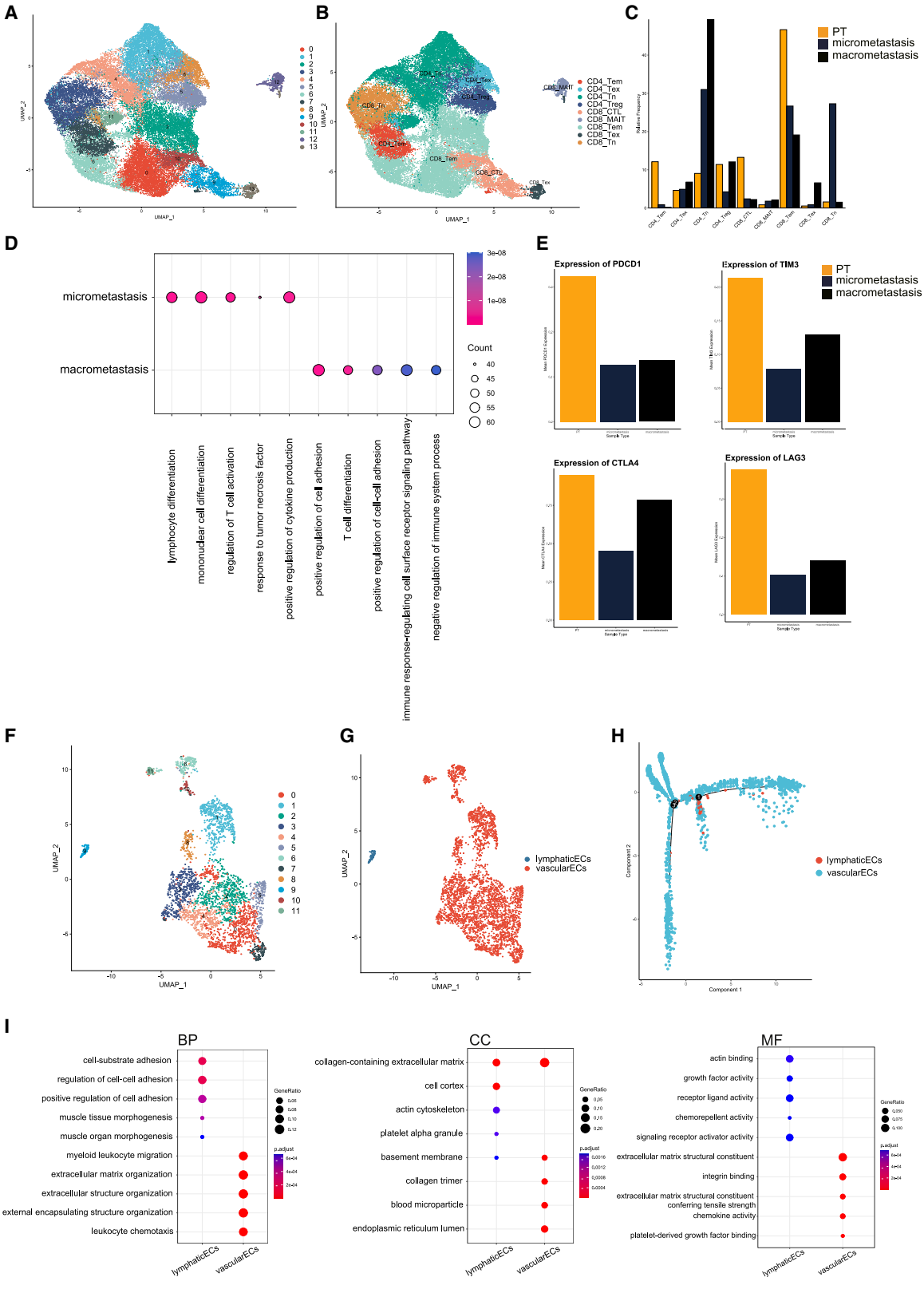

(legend on next page)

way for CTCs. This shift likely enhances the survival of CTCs in the circulatory system, aiding in their successful metastasis.[17] Another study also noted that invasive cancer cells utilize the transcription coactivator peroxisome proliferator-activated receptor gamma coactivator 1 alpha (PGC-1α) to enhance mitochondrial oxidative phosphorylation, thereby promoting distal metastasis.[18] The similar oxidative phosphorylation pattern observed in MME cells suggests that this metabolic switch may be a widespread strategy cancer cells employ during metastasis, with MME potentially serving as precursor cells to CTCs. This metabolic shift may, therefore, begin even before metastasis is initiated. The shared metabolic characteristics between CTCs and MME cells provide new insights into the mechanisms of tumor metastasis and highlight the importance of targeting oxidative phosphorylation as a potential therapeutic approach for advanced GC.

GC is a highly heterogeneous malignancy, and its diverse and complex metabolic landscape makes it difficult to understand its clinical and biological implications.[19] Our study used scRNA-seq technology to characterize GC's heterogeneity and metabolic alterations from primary to metastatic sites. We found that oxidative phosphorylation increased first and then decreased in metastatic MME cells, while the opposite trend was observed in PT cells. We intersected two oxidative phosphorylation gene sets with MME marker genes to identify critical genes driving this metabolic transformation, screening 32 candidate genes. We ultimately found that ATP5MC2's pseudotemporal trajectory was highly consistent with the oxidative phosphorylation pathway and significantly correlated with GC prognosis. IHC cohort analysis further confirmed that high ATP5MC2 expression was associated with GC metastasis. Both *in vitro* and *in vivo* experiments demonstrated that overexpression of ATP5MC2 enhances the proliferation, migration, and invasion capabilities of GC cells, highlighting ATP5MC2's crucial role in promoting metastasis. As a subunit encoding mitochondrial ATP synthase, ATP5MC2 catalyzes ATP synthesis during oxidative phosphorylation by utilizing the electrochemical gradient created by protons across the inner membrane.[20] Previous studies, consistent with ours, have shown that the oxidative phosphorylation pathway promotes cell invasion, possibly due to increased mitochondrial superoxide production resulting from hyperactive mitochondrial metabolism.[21]

Our findings expand upon Otto Heinrich Warburg's original description of cancer's metabolic reprogramming.[22] The upregulation of ATP5MC2 in metastatic GC, enhanced oxidative phosphorylation, and reduced glycolysis may strengthen metastatic cancer cells' survival in the circulatory system, facilitating successful metastasis. On the other hand, this metabolic change might be part of a self-protection mechanism where tumor cells mimic normal cells to evade immune surveillance and clearance, enabling smooth metastasis and colonization. Whether this metabolic switch is primarily due to tumor cells' disguise requires further research for deeper exploration and verification. Using our scRNA dataset and an external validation set, we observed that epithelial cells exhibit higher ATP5MC2 expression at the transcriptome level compared to most other cell types (Figures S2H–S2J). Additionally, the heterogeneity in ATP5MC2 expression among epithelial cells may reflect the presence of distinct subsets, including oxidative phosphorylation-dependent normal epithelial cells, glycolysis-prone tumor cells, and early metastatic cells with upregulated oxidative phosphorylation. Interestingly, ATP5MC2 expression in other cell types was not significantly lower than in epithelial cells. We speculate that although ATP5MC2 is transcribed across all cell types, post-transcriptional modifications may suppress its protein levels in non-epithelial cells. In epithelial cells, such regulatory mechanisms might be absent or aligned with their metabolic demands, allowing ATP5MC2 to be detectable at the protein level. Previous studies have also shown that the expression of ATP synthase catalytic subunits is tightly regulated at the post-transcriptional level, with miRNAs playing a critical role in the post-transcriptional regulation of these subunits.[23]

In addition, we identified the influence of different immune response patterns and microenvironmental characteristics of each subtype on tumor metastasis in the TME, highlighting the complex cell-cell interactions that drive tumor progression and metastasis.[24] Through the CellChat analysis, we first found that metastases had more active and heterogeneous microenvironment features than primary sites, including an increase in the number and strength of cell-cell interactions, a more active role of immune cells as signal inputs and outputs, and a significant increase in information flow. This aroused our interest to further explore the microenvironment related to GC metastasis. Specifically, we identified, for the first time, the differential expression of distinct T cell exhaustion states and immune checkpoint molecules across various stages of metastasis. This finding suggests a dynamic interaction between tumor cells and immune cells that may facilitate immune evasion and promote successful tumor metastasis. These observations were further validated through multicolor fluorescence experiments using clinical samples. To date, there are no reports on the molecular dynamics of immune checkpoints during T cell involvement in metastasis. Our study provides a foundational reference for future investigations in this area. By analyzing the

Figure 7. T cell dynamics and endothelial cell contributions across metastasis stages

(A) UMAP plot presenting 14 distinct T cell clusters.
(B) UMAP plot presenting nine distinct T cell types.
(C) The bar chart shows the proportion of different types of T cells in different stages of metastasis.
(D) GO analysis of T cells between micro-metastasis and macro-metastasis.
(E) Expression of immune checkpoint molecules in T cells at different metastasis stages.
(F) UMAP plot presenting 12 distinct endothelial cell clusters.
(G) UMAP plot presenting lymphatic endothelial cells and vascular endothelial cells.
(H) Pseudotime analysis shows the evolutionary trajectory of endothelial cells, colored by cell locations.
(I) GO analysis between lymphatic endothelial cells and vascular endothelial cells.

microenvironment of different subtypes of GC samples, we found that the unique characteristics of lymphatic endothelial cells may be the potential cause of tumor metastasis through lymphatic vessels. In our previous findings, we observed robust cellular communication between T cells and B cells. Furthermore, we identified increased germinal center B cell infiltration in patients with EBV-positive GC, which may be linked to an enhanced response to immunotherapy.[25] Additionally, we observed heterogeneity in the distribution of TAMs across different GC subtypes. The imbalance between pro-inflammatory and anti-inflammatory TAM subtypes contributed to variations in angiogenesis, immune responses, and inflammatory factor secretion, ultimately influencing patient prognosis. We also explored the distribution and function of the CAF subtype, and consistent with previous studies, our findings highlight the potential promoting effect of specific CAF subgroups on GC metastasis.[26]

In conclusion, our study provides valuable insights into GC metastasis's metabolic and immune landscape, identifying ATP5MC2 as a potential therapeutic target. These findings enhance our understanding of metabolic changes in metastasis and could inform the development of more effective therapies for advanced GC.

Limitations of the study

This study has some limitations. First is the sample size, particularly the limited number of metastatic samples, which may affect the generalizability of our findings. Additionally, while scRNA-seq provides high-resolution insights into cellular heterogeneity, it does not capture the spatial context of these cells within the TME. Future studies could address these limitations by incorporating larger cohorts and employing spatial transcriptomics to understand better the spatial relationships between tumor and immune cells in metastatic niches.[27,28]

RESOURCE AVAILABILITY

Lead contact

Further information and requests for resources and reagents should be directed to and will be fulfilled by the lead contact, Qingling Zhang (zhangqingling@gdph.org.cn).

Materials availability

This study did not generate new unique reagents.

Data and code availability

All raw data are publicly accessible in the Genome Sequence Archive for Human (GSA-Human) at the National Genomics Data Center under the accession number HRA009590 (http://bigd.big.ac.cn/gsa-human). All original code is available in this paper's supplemental information. Any additional information required to reanalyze the data reported in this paper is available from the lead contact upon request.

ACKNOWLEDGMENTS

This project was supported by grants of the National Natural Science Foundation of China (Q.Z., 8197227 and 82173033 and Yangwei Xu, 82102712), China Postdoctoral Science Foundation (Yangwei Xu, 2021M690751), Key Area Research and Development Program of Guangdong Province (2021B0101420005), High-level Hospital Construction Project (Q.Z., DFJHBF202108 and YKY-KF202204), and Guangdong Provincial Key Laboratory of Artificial Intelligence in Medical Image Analysis and Application (2022B1212010011).

AUTHOR CONTRIBUTIONS

Q.Z. and R.Z. designed the study and prepared the manuscript. R.Z. performed the scRNA-seq data analysis and statistical analyses. R.Z. and Z.L. performed experiments. Y.L., W.L., and W.H. assisted in carrying out the experiments. Y.H., X.L., and Z.L. assisted in IHC and H&E staining. R.Z. and Q.Z. wrote the manuscript, and all authors contributed to writing and providing feedback.

DECLARATION OF INTERESTS

The authors declare no competing interests.

STAR★METHODS

Detailed methods are provided in the online version of this paper and include the following:

- KEY RESOURCES TABLE
- EXPERIMENTAL MODEL AND STUDY PARTICIPANT DETAILS
  - Human Gastric cancer samples
  - External datasets
  - Cell lines
  - Animal subjects
- METHOD DETAILS
  - Library preparation and sequencing of single cell RNA-seq
  - Data preprocessing and quality control for scRNA-Seq data
  - Screening of marker genes in each cluster and annotation of cell types
  - Identified malignant epithelial cells by copy number variation analysis
  - Pseudotime analysis revealed cell evolution trajectory and gene expression changes
  - Analysis of cell-cell interaction networks
  - Kaplan-Meier (KM) survival analysis
  - Gene Set Variation Analysis
  - Gene ontology enrichment analysis
  - Multiplex immunofluorescence
  - Immunohistochemistry
  - RNA extraction and quantitative real-time PCR (RT-qPCR)
  - Western blot
  - Construction of stable ATP5MC2-knockdown and ATP5MC2-overexpress cell lines
  - Cell proliferation assay
  - Cell migration and invasion assay
  - Clonal formation assay
  - Xenograft mouse model
  - Lung metastasis model via tail vein injection
- QUANTIFICATION AND STATISTICAL ANALYSIS

SUPPLEMENTAL INFORMATION

Supplemental information can be found online at https://doi.org/10.1016/j.isci.2025.112296.

Received: September 4, 2024
Revised: December 11, 2024
Accepted: March 24, 2025
Published: March 27, 2025

REFERENCES

1. Lin, J.L., Lin, J.X., Lin, G.T., Huang, C.M., Zheng, C.H., Xie, J.W., Wang, J.B., Lu, J., Chen, Q.Y., and Li, P. (2024). Global incidence and mortality

trends of gastric cancer and predicted mortality of gastric cancer by 2035. BMC Public Health *24*, 1763. https://doi.org/10.1186/s12889-024-19104-6.

2. Cao, W., Chen, H.D., Yu, Y.W., Li, N., and Chen, W.Q. (2021). Changing profiles of cancer burden worldwide and in China: a secondary analysis of the global cancer statistics 2020. Chin. Med. J. *134*, 783–791. https://doi.org/10.1097/cm9.0000000000001474.
3. Allemani, C., Matsuda, T., Di Carlo, V., Harewood, R., Matz, M., Nikšić, M., Bonaventure, A., Valkov, M., Johnson, C.J., Estève, J., et al. (2018). Global surveillance of trends in cancer survival 2000-14 (CONCORD-3): analysis of individual records for 37 513 025 patients diagnosed with one of 18 cancers from 322 population-based registries in 71 countries. Lancet *391*, 1023–1075. https://doi.org/10.1016/s0140-6736(17)33326-3.
4. Koppenol, W.H., Bounds, P.L., and Dang, C.V. (2011). Otto Warburg's contributions to current concepts of cancer metabolism. Nat. Rev. Cancer *11*, 325–337. https://doi.org/10.1038/nrc3038.
5. Li, Y.L., Chen, C.H., Chen, J.Y., Lai, Y.S., Wang, S.C., Jiang, S.S., and Hung, W.C. (2020). Single-cell analysis reveals immune modulation and metabolic switch in tumor-draining lymph nodes. OncoImmunology *9*, 1830513. https://doi.org/10.1080/2162402x.2020.1830513.
6. Lin, S.C., and Hardie, D.G. (2018). AMPK: Sensing Glucose as well as Cellular Energy Status. Cell Metab. *27*, 299–313. https://doi.org/10.1016/j.cmet.2017.10.009.
7. Jovic, D., Liang, X., Zeng, H., Lin, L., Xu, F., and Luo, Y. (2022). Single-cell RNA sequencing technologies and applications: A brief overview. Clin. Transl. Med. *12*, e694. https://doi.org/10.1002/ctm2.694.
8. Franzén, O., Gan, L.M., and Björkegren, J.L.M. (2019). PanglaoDB: a web server for exploration of mouse and human single-cell RNA sequencing data. Database *2019*, baz046. https://doi.org/10.1093/database/baz046.
9. Sánchez-Ponce, Y., and Fuentes-Pananá, E.M. (2021). The Role of Coinfections in the EBV-Host Broken Equilibrium. Viruses *13*, 1399. https://doi.org/10.3390/v13071399.
10. Qiu, M.Z., Wang, C., Wu, Z., Zhao, Q., Zhao, Z., Huang, C.Y., Wu, W., Yang, L.Q., Zhou, Z.W., Zheng, Y., et al. (2023). Dynamic single-cell mapping unveils Epstein–Barr virus-imprinted T-cell exhaustion and on-treatment response. Signal Transduct. Target. Ther. *8*, 370. https://doi.org/10.1038/s41392-023-01622-1.
11. Ajani, J.A., D'Amico, T.A., Bentrem, D.J., Chao, J., Cooke, D., Corvera, C., Das, P., Enzinger, P.C., Enzler, T., Fanta, P., et al. (2022). Gastric Cancer, Version 2.2022, NCCN Clinical Practice Guidelines in Oncology. J. Natl. Compr. Canc. Netw. *20*, 167–192. https://doi.org/10.6004/jnccn.2022.0008.
12. Gerstberger, S., Jiang, Q., and Ganesh, K. (2023). Metastasis. Cell *186*, 1564–1579. https://doi.org/10.1016/j.cell.2023.03.003.
13. Li, Z., and Zhang, H. (2016). Reprogramming of glucose, fatty acid and amino acid metabolism for cancer progression. Cell. Mol. Life Sci. *73*, 377–392. https://doi.org/10.1007/s00018-015-2070-4.
14. Jung, J., Zeng, H., and Horng, T. (2019). Metabolism as a guiding force for immunity. Nat. Cell Biol. *21*, 85–93. https://doi.org/10.1038/s41556-018-0217-x.
15. Nguyen, D.X., Bos, P.D., and Massagué, J. (2009). Metastasis: from dissemination to organ-specific colonization. Nat. Rev. Cancer *9*, 274–284. https://doi.org/10.1038/nrc2622.
16. Lawson, D.A., Kessenbrock, K., Davis, R.T., Pervolarakis, N., and Werb, Z. (2018). Tumour heterogeneity and metastasis at single-cell resolution. Nat. Cell Biol. *20*, 1349–1360. https://doi.org/10.1038/s41556-018-0236-7.
17. Liu, Y., Zhang, Z., Wang, J., Chen, C., Tang, X., Zhu, J., and Liu, J. (2019). Metabolic reprogramming results in abnormal glycolysis in gastric cancer: a review. OncoTargets Ther. *12*, 1195–1204. https://doi.org/10.2147/ott.S189687.
18. LeBleu, V.S., O'Connell, J.T., Gonzalez Herrera, K.N., Wikman, H., Pantel, K., Haigis, M.C., de Carvalho, F.M., Damascena, A., Domingos Chinen, L.T., Rocha, R.M., et al. (2014). PGC-1α mediates mitochondrial biogenesis and oxidative phosphorylation in cancer cells to promote metastasis. Nat. Cell Biol. *16*, 992–1003. https://doi.org/10.1038/ncb3039.
19. Chen, H., Jing, C., Shang, L., Zhu, X., Zhang, R., Liu, Y., Wang, M., Xu, K., Ma, T., Jing, H., et al. (2024). Molecular characterization and clinical relevance of metabolic signature subtypes in gastric cancer. Cell Rep. *43*, 114424. https://doi.org/10.1016/j.celrep.2024.114424.
20. He, J., Ford, H.C., Carroll, J., Ding, S., Fearnley, I.M., and Walker, J.E. (2017). Persistence of the mitochondrial permeability transition in the absence of subunit c of human ATP synthase. Proc. Natl. Acad. Sci. USA *114*, 3409–3414. https://doi.org/10.1073/pnas.1702357114.
21. Porporato, P.E., Payen, V.L., Pérez-Escuredo, J., De Saedeleer, C.J., Danhier, P., Copetti, T., Dhup, S., Tardy, M., Vazeille, T., Bouzin, C., et al. (2014). A mitochondrial switch promotes tumor metastasis. Cell Rep. *8*, 754–766. https://doi.org/10.1016/j.celrep.2014.06.043.
22. Vander Heiden, M.G., Cantley, L.C., and Thompson, C.B. (2009). Understanding the Warburg effect: the metabolic requirements of cell proliferation. Science *324*, 1029–1033. https://doi.org/10.1126/science.1160809.
23. Willers, I.M., Martínez-Reyes, I., Martínez-Diez, M., and Cuezva, J.M. (2012). miR-127-5p targets the 3'UTR of human β-F1-ATPase mRNA and inhibits its translation. Biochim. Biophys. Acta *1817*, 838–848. https://doi.org/10.1016/j.bbabio.2012.03.005.
24. Qian, Y., Zhai, E., Chen, S., Liu, Y., Ma, Y., Chen, J., Liu, J., Qin, C., Cao, Q., Chen, J., and Cai, S. (2022). Single-cell RNA-seq dissecting heterogeneity of tumor cells and comprehensive dynamics in tumor microenvironment during lymph nodes metastasis in gastric cancer. Int. J. Cancer *151*, 1367–1381. https://doi.org/10.1002/ijc.34172.
25. Sakimura, C., Tanaka, H., Okuno, T., Hiramatsu, S., Muguruma, K., Hirakawa, K., Wanibuchi, H., and Ohira, M. (2017). B cells in tertiary lymphoid structures are associated with favorable prognosis in gastric cancer. J. Surg. Res. *215*, 74–82. https://doi.org/10.1016/j.jss.2017.03.033.
26. Chen, B., Liu, X., Yu, P., Xie, F., Kwan, J.S.H., Chan, W.N., Fang, C., Zhang, J., Cheung, A.H.K., Chow, C., et al. (2023). H. pylori-induced NF-κB-PIEZO1-YAP1-CTGF axis drives gastric cancer progression and cancer-associated fibroblast-mediated tumour microenvironment remodelling. Clin. Transl. Med. *13*, e1481. https://doi.org/10.1002/ctm2.1481.
27. Wang, F., Long, J., Li, L., Wu, Z.X., Da, T.T., Wang, X.Q., Huang, C., Jiang, Y.H., Yao, X.Q., Ma, H.Q., et al. (2023). Single-cell and spatial transcriptome analysis reveals the cellular heterogeneity of liver metastatic colorectal cancer. Sci. Adv. *9*, eadf5464. https://doi.org/10.1126/sciadv.adf5464.
28. Zhang, Q., Abdo, R., Iosef, C., Kaneko, T., Cecchini, M., Han, V.K., and Li, S.S.C. (2022). The spatial transcriptomic landscape of non-small cell lung cancer brain metastasis. Nat. Commun. *13*, 5983. https://doi.org/10.1038/s41467-022-33365-y.
29. Butler, A., Hoffman, P., Smibert, P., Papalexi, E., and Satija, R. (2018). Integrating single-cell transcriptomic data across different conditions, technologies, and species. Nat. Biotechnol. *36*, 411–420. https://doi.org/10.1038/nbt.4096.
30. Patel, A.P., Tirosh, I., Trombetta, J.J., Shalek, A.K., Gillespie, S.M., Wakimoto, H., Cahill, D.P., Nahed, B.V., Curry, W.T., Martuza, R.L., et al. (2014). Single-cell RNA-seq highlights intratumoral heterogeneity in primary glioblastoma. Science *344*, 1396–1401. https://doi.org/10.1126/science.1254257.
31. Trapnell, C., Cacchiarelli, D., Grimsby, J., Pokharel, P., Li, S., Morse, M., Lennon, N.J., Livak, K.J., Mikkelsen, T.S., and Rinn, J.L. (2014). The dynamics and regulators of cell fate decisions are revealed by

pseudotemporal ordering of single cells. Nat. Biotechnol. *32*, 381–386. https://doi.org/10.1038/nbt.2859.

32. Jin, S., Plikus, M.V., and Nie, Q. (2025). CellChat for systematic analysis of cell-cell communication from single-cell transcriptomics. Nat. Protoc. *20*, 180–219. https://doi.org/10.1038/s41596-024-01045-4.

33. Jin, S., Guerrero-Juarez, C.F., Zhang, L., Chang, I., Ramos, R., Kuan, C.H., Myung, P., Plikus, M.V., and Nie, Q. (2021). Inference and analysis of cell-cell communication using CellChat. Nat. Commun. *12*, 1088. https://doi.org/10.1038/s41467-021-21246-9.

34. Hänzelmann, S., Castelo, R., and Guinney, J. (2013). GSVA: gene set variation analysis for microarray and RNA-seq data. BMC Bioinf. *14*, 7. https://doi.org/10.1186/1471-2105-14-7.

35. Yu, G., Wang, L.G., Han, Y., and He, Q.Y. (2012). clusterProfiler: an R package for comparing biological themes among gene clusters. OMICS *16*, 284–287. https://doi.org/10.1089/omi.2011.0118.

36. Naito, S., von Eschenbach, A.C., Giavazzi, R., and Fidler, I.J. (1986). Growth and metastasis of tumor cells isolated from a human renal cell carcinoma implanted into different organs of nude mice. Cancer Res. *46*, 4109–4115.

STAR★METHODS

KEY RESOURCES TABLE

REAGENT or RESOURCE	SOURCE	IDENTIFIER
Antibodies		
ATP5MC2	Abcam	Cat# AB180149
CD3	Abcam	Cat# AB307134
SMA	Abcam	Cat# AB184675; RRID: AB_2832195
PanCK	Cell Signaling Technology	Cat# 4523S; RRID: AB_836889
CD20	eBioscience	Cat# 53-0202-82; RRID: AB_10734358
PD1	HUABIO	ET1606-41; RRID: AB_3069736
CTLA4	HUABIO	HA721269; RRID: AB_3072386
LAG3	HUABIO	HA721358; RRID: AB_3072475
TIM3	HUABIO	EM1701-19; RRID: AB_3068747
GAPDH	proteintech	Cat# 60004-1-Ig; RRID: AB_2107436
CoraLite488-conjugated Goat Anti-Rabbit IgG	proteintech	Cat# SA00013-2; RRID: AB_2797132
CoraLite594 – conjugated Goat Anti-Mouse IgG	proteintech	Cat# SA00013-3, RRID: AB_2797133
IHC secondary antibody	ZSGB-BIO	Cat# PV-6001
Bacterial and virus strains		
Lentivirus knockdown vector (hU6-ATP5MC2-CMV- fLuc -PGK-Puro)	GENEYUAN	N/A
Lentivirus overexpression vector (PCDH-CMV-ATP5MC2-P2A-fLuc-EF1a- T2A-Puro-WPRE)	HanYi Bio	N/A
Biological samples		
Fresh and FFPE gastric cancer samples	Guangdong Provincial People's Hospital	N/A
Chemicals, peptides, and recombinant proteins		
Cell counting kit-8	EZbioscience	Cat# EZB-CK8
EDTA buffer	Biosharp	Cat# BL617A
DAB	ZSGB-BIO	Cat# ZLI-9019
RT Mix	Accurate Biology	Cat# AG11706
SYBR Green	Accurate Biology	Cat# AG11759
Matrigel	Corning	Cat# 354248
Critical commercial assays		
EZ-Press RNA Purification Assay	EZbioscience	Cat# B0004DP
IHC kit	ZSGB-BIO	Cat# ZLI-9019
ATP Assay Kit	Beyotime	Cat# S0026
Deposited data		
TCGA-STAD	TCGA	https://portal.gdc.cancer.gov/
Gastric cancer single cell sequencing data (HRA009590)	GSA	https://ngdc.cncb.ac.cn/gsa-human/
Experimental models: Cell lines		
HGC27	ATCC	RRID: CVCL_1279
MKN45	ATCC	RRID: CVCL_0434
AGS	ATCC	RRID: CVCL_0139
N87	ATCC	RRID: CVCL_1603

(*Continued on next page*)

Continued

REAGENT or RESOURCE	SOURCE	IDENTIFIER
Experimental models: Organisms/strains		
BALB/c nude mice (nu/nu)	Guangdong Medical Laboratory Animal Center	N/A
Oligonucleotides		
See **Methods- RNA extraction and quantitative real-time PCR** for oligonucleotide information	This paper	N/A
Software and algorithms		
R	R Foundation	https://www.r-project.org/
GraphPad Prism	GraphPad Software, Inc.	https://www.graphpad.com
ImageJ	National Institutes of Health (NIH)	https://imagej.nih.gov/ij/

EXPERIMENTAL MODEL AND STUDY PARTICIPANT DETAILS

Human Gastric cancer samples

For single-cell analysis, 12 patients diagnosed with GC were enrolled in this study. The collected specimens comprised 11 primary gastric tumor tissues (PT), 7 lymph nodes (LNs), and 1 OM. Detailed clinical and pathological data are documented in Table S1. Additionally, 33 FFPE GC samples and paired lymph nodes were collected, with patient details documented in Table S2. Ethical approval for this study was obtained from the Ethics Committee of Guangdong Provincial People's Hospital (ID: 2020-271H-1). All participants provided informed consent prior to surgery and had not received any treatment prior to the collection of samples.

External datasets

The external validation GC scRNA-seq data GSE163558 was downloaded via Gene Expression Omnibus (GEO). And the transcriptome RNA sequencing (RNA-seq) data of human GC samples was downloaded via The Cancer Genome Atlas (https://portal.gdc.cancer.gov/). All the RNA-seq data selected in our study were normalized by fragments per kilobase million. After removing duplications and samples that were missing data, the RNA-seq dataset consisted of 20 normal samples and 293 cancer samples and matched the clinical information of the selected data.

Cell lines

The human GC cell lines HGC27, MKN45, AGS, and N87 were obtained from the American Type Culture Collection. All of the cell lines were authenticated and tested for mycoplasma contamination and cultured in DMEM full medium with 10% FBS with 10% FBS at 37°C in a humidified.

Animal subjects

Three-week-old female BALB/c nude mice were used to establish xenograft and lung metastasis models.

METHOD DETAILS

Library preparation and sequencing of single cell RNA-seq

Single cells were processed using the Chromium Single Cell 5′ Gel Bead, Chip, and Library Kits v2 (10X Genomics) according to the manufacturer's instructions within the Chromium Single Cell Gene Expression Solution. Each channel was loaded with approximately 8000–10000 total cells, yielding an average cell recovery. Within the Chromium instrument, cells were encapsulated into Gel Beads in Emulsion, where cell lysis and barcoded reverse transcription of mRNA took place. This step was followed by mRNA amplification, shearing, and attachment of 5′ adaptors and sample indices. The libraries were then sequenced on an MGISEQ-2000 at BGI in Beijing, China, producing an average of 200 Gb of raw data per sample.

Data preprocessing and quality control for scRNA-Seq data

Data preprocessing was performed using the "Seurat" package (version 4.2.3),[29] where criteria were applied to tumor samples as follows: nFeature_RNA >200, nCount_RNA >2000, and mitochondrial genes below 20%. This preprocessing yielded 92,842 cells suitable for downstream analysis. The normalization of count data was achieved using the "NormalizeData" function. The top 2000 highly variable genes (HVGs) were subsequently identified with the "FindVariableGenes" function, followed by principal component analysis performed on these genes. The optimal number of principal components for further analysis was determined using the

"ElbowPlot" function, as recommended by Seurat. Visualization was facilitated by Uniform Manifold Approximation and Projection (UMAP) using the "RunUMAP" function with default parameters. Single-cell clustering by expression profiles was conducted using the "FindClusters" function at a resolution of 0.5.

Screening of marker genes in each cluster and annotation of cell types

Marker genes within each cluster were identified using the "FindAllMarkers" function in Seurat. Cell-type identification was based on lineage-specific markers to categorize cells at the major cell type level. T cells and NK cells were further differentiated based on the average expression of specific marker genes: T cells expressed CD3D, CD3E, and CD2, whereas NK cells expressed KLRD1, NKG7, and GNLY. B cells and Plasma B cells were distinguished as B cells expressed CD79A, MS4A1, and IGHD, while Plasma B cells expressed MZB1, IGHA2, and SDC1. Epithelial cells were identified by expressions of EPCAM, KRT18, and GKN1; fibroblast cells by DCN, COL1A1, and COL1A2; endothelial cells by VWF, ENG, and FLT1; and myeloid cells by IL-1β, S100A8, and TREM1.

Identified malignant epithelial cells by copy number variation analysis

The ‘‘inferCNV’’ package (version 1.12.0; https://github.com/broadinstitute/inferCNV/wiki)[30] was employed to calculate CNV levels for each cell across various chromosome regions within clusters of epithelial cells to pinpoint malignant epithelial cells. Fibroblast cells served as control cells, and the random seed was set to 123 to ensure reproducibility. Normal epithelial cells and cancer cells were differentiated by comparing CNV scores, which quantify CNV magnitude.

Pseudotime analysis revealed cell evolution trajectory and gene expression changes

The "monocle2" package (version 2.26.0)[31] was utilized to sequence individual cells in pseudotime, exploiting the asynchronous processes of individual cells and positioning them along trajectories representing biological processes. The "newCellDataSet()" function in monocle2 was used to construct a CellDataSet object from the Seurat object. Size factors normalized mRNA differences between cells, with HVGs selected based on monocle criteria. Dimension reduction analysis was performed, and the specified cell cluster was designated as the root node for pseudotime ordering of cells of interest, culminating in plotting pseudotime trajectories for different cells, genes, and pathways.

Analysis of cell-cell interaction networks

To investigate cell-to-cell interaction between the tumor and non-malignant cells, ‘‘CellChat’’ R package and ‘‘CellPhoneDB’’ database were applied.[32,33] We use the "createCellChat" function to create the "CellChat" object, The "computeCommunProb", "computeCommunProbPathway" and "filterCommunication" and "aggregateNet" functions are used to infer the cellular communication network. netVisual_circle and netVisual_heatmap are used. "netAnalysis_signalingRole_heatmap" and "netAnalysis_signalingRole_scatter" to visualize cross-talk between cells and cross-talk differences between different groups.

Kaplan-Meier (KM) survival analysis

The ‘‘org.hs.e.g.,.db’’ package was used to convert the Ensembl ID into a gene symbol. Kaplan-Meier (KM) survival curves for ATP5MC2 high- and low-expression groups were generated using the ‘‘survival’’ and ‘‘survminer’’ packages, with the "best cutoff" method applied to determine the optimal threshold for grouping based on expression levels.

Gene Set Variation Analysis

GSVA was performed to identify pathways and cellular processes differentially enriched across various clusters using the "GSVA" package (version 1.44.5).[34]

Gene ontology enrichment analysis

GO enrichment analysis was conducted to compare $CD8^+$ T cells from macro- and micro-metastases, as well as between lymphatic endothelial cells and vascular endothelial cells, using the "clusterProfiler" package (version 4.4.4),[35] the results for which adjust p-value <0.05 were considered statistically significant.

Multiplex immunofluorescence

Multiplex immunofluorescence analyses were conducted on tumor cells expressing ATP5MC2 and other cellular components within the TME using the ZellScanner ONE multiplex imaging platform (S/*N* 3869002076, Zellkraftwerk, Hannover, Germany). For detailed procedures, please refer to the product manual. GC tissue sections were sequentially stained with various primary antibodies, including ATP5MC2 (Abcam, AB180149), PanCK (Cell Signaling Technology, 4523S), CD3 (Abcam, AB307134), CD20 (eBioscience, 2608794), SMA (Abcam, AB184675), PD1 (HUABIO, ET1606-41), CTLA4 (HUABIO, HA721269), LAG3 (HUABIO, HA721358), and TIM3 (HUABIO, EM1701-19). After primary incubation, ATP5MC2 was further incubated with fluorescence-conjugated secondary antibody (proteintech, SA00013-2 and SA00013-3), while the remaining markers used fluorescence-conjugated primary antibodies and did not require secondary antibody incubation. Nuclei were counterstained with 4′,6-diamidino-2-phenylindole (DAPI, Solarbio, C0065) following the labeling of all human antigens.

Immunohistochemistry

Immunohistochemical staining was performed to assess ATP5MC2 expression in GC and lymph node tissues. Sections of formalin-fixed, paraffin-embedded tissues from GC and associated lymph nodes were sectioned at 5 μm thickness and mounted on adhesion microscope slides. The slides were deparaffinized in xylene and rehydrated through a series of graded alcohols. Endogenous peroxidase activity was quenched using 3% hydrogen peroxide in methanol for 10 min at room temperature. Antigen retrieval was carried out in a pressure cooker using pH 9.0 EDTA buffer (Biosharp, BL617A) for 15 min.

After antigen retrieval, sections were incubated overnight at 4°C with a rabbit polyclonal antibody against ATP5MC2 (Abcam, AB180149) at a dilution of 1:500. Following primary antibody incubation, sections were washed thrice in phosphate-buffered saline (PBS) and then incubated with a secondary antibody (ZSGB-BIO, PV-6001) for 60 min at room temperature. Unbound secondary antibodies were thoroughly washed off with PBS. Visualization was achieved using 3,3′-diaminobenzidine (DAB) (ZSGB-BIO, ZLI-9019) as the chromogen. Finally, sections were counterstained with hematoxylin, dehydrated, and mounted.

RNA extraction and quantitative real-time PCR (RT-qPCR)

The total RNA of tumor tissues and adjacent normal tissues was extracted using the EZ-Press RNA Purification Kit (EZbioscience, B0004DP). cDNA was obtained by reverse transcription using the RT Mix (Accurate Biology, AG11706). Based on the SYBR Green (Accurate Biology, AG11759) method, the LightCycler 480 II real-time PCR system (Roche, Swiss) was used for RT–qPCR detection. After the expression level of GAPDH was used for normalization, the relative expression level of mRNA was determined. The mRNA-specific primer sequences were as follows: ATP5MC2-F: CTGCTCCAAGTTTGTCTCC, ATP5MC2-R: TCAGTATCTCCGGTCGTTT, GAPDH-F: ATGACATCAAGAAGGTGGTG, GAPDH-R: CATACCAGGAAATGAGCTTG.

Western blot

Proteins were denatured, separated by SDS-PAGE, and subsequently transferred to PVDF membranes (Merck, USA). The membranes were then blocked with skimmed milk before incubation with primary antibodies (ATP5MC2, Abcam, AB180149; GAPDH, proteintech, 60004-1-Ig) followed by secondary antibodies. Protein visualization was performed using a GelView 6000 Plus (BLT Photon Technology, China), adhering strictly to the manufacturer's instructions.

Construction of stable ATP5MC2-knockdown and ATP5MC2-overexpress cell lines

The lentivirus knockdown vector (LV-shATP5MC2-Puro) was synthesized by GENEYUAN (Guangzhou, China). The lentivirus overexpression vector was synthesized by HanYi Bio (Guangzhou, China). The cell transfection was conducted according to the instruction manual and subsequently selected with puromycin (2.5 μg/mL) for ~7 days to establish the stable knockdown and overexpression of cell lines. RT-qPCR and Western blot were used to verify the interference efficiency of the stable ATP5MC2-knockdown and ATP5MC2-overexpression cell lines. ATP Assay Kit (Beyotime, S0026) was used to detect intracellular ATP content in GC cells with ATP5MC2 knockdown and overexpression.

Cell proliferation assay

Cell suspensions were seeded in a 96-well plate at a density of 1,000 cells per well, with three replicates per group. At 24, 48, 72, and 96 h after seeding, 100 μL of CCK-8 solution (EZbioscience, EZB-CK8) was added to each well. The plate was then incubated at 37°C for 2 h. Absorbance was measured at 450 nm using an Epoch Biotek Microplate Reader (Epoch Biotek, USA).

Cell migration and invasion assay

A total of 1×10^5 cells were seeded into Transwell chambers (Corning, USA), with or without Matrigel (Corning, 354248), at a volume of 200 μL per chamber. The chambers were incubated for 24 to 72 h at 37°C. Cells were then fixed with paraformaldehyde for 15 min and stained with crystal violet for an additional 15 min. After washing away excess stain with PBS, cell migration and invasion from the upper to the lower chamber were observed. Once the chambers were completely dried, the migrated and invaded cells were photographed and quantified using ImageJ.

Clonal formation assay

Cell suspensions were seeded in a 6-well plate at a density of 200 cells per well with three replicates per group and cultured for 14 days until visible colonies formed. Colonies were fixed with paraformaldehyde for 15 min and subsequently stained with crystal violet for 15 min. The excess stain was washed away with PBS. After drying the plates completely, colonies were photographed and quantified using ImageJ.

Xenograft mouse model

Female BALB/c nude mice, 3 weeks old, were maintained under specific pathogen-free (SPF) conditions at the Guangdong Medical Laboratory Animal Center. Cell suspensions of HGC27 and MKN45 cells were prepared at a concentration of 1.5×10^7 cells per mL. Each mouse received a 200 μL subcutaneous injection under the skin of the leg. The mice were monitored for 4 weeks, after which they were euthanized, and the tumors were excised. Tumor dimensions were measured using vernier calipers, and volumes were calculated using the formula: tumor volume (mm^3) = (length × $width^2$)/2.[36]

Lung metastasis model via tail vein injection

Female BALB/c nude mice, 3 weeks old, were maintained under SPF conditions at the Guangdong Medical Laboratory Animal Center. The density of MKN45 cell suspensions was adjusted to 1×10^7 cells per mL, with a total injection volume of 100 μL per mouse. The suspension was thoroughly mixed and filtered through a cell sieve to minimize the risk of embolism. The prepared cells were then injected into the mice via the tail vein at a rate of 100 μL per injection. Four weeks after injection, luciferase substrates were given, and *in vivo*, imaging was performed to assess lung metastasis.

QUANTIFICATION AND STATISTICAL ANALYSIS

The statistical test methods are provided in the corresponding figure legends or Methods section. Statistical analyses were performed using R 4.2.1 and GraphPad Prism 9.5 (GraphPad Software, Inc.). Continuous variables are presented as mean ± SD for normally distributed data or median (interquartile range, IQR) for non-normally distributed data, while categorical variables are expressed as numbers (percentages). The Wilcoxon rank-sum test was used to compare continuous variables between two independent groups, and categorical data were analyzed using the t-test. Unless otherwise specified, p-values <0.05 were considered statistically significant. n represents the number per group (cases or animals), and error bars in the figures indicate the standard deviation.